

UC Merced

UC Merced Previously Published Works

Title

Deformation Rate-Adaptive Conducting Polymers and Composites

Permalink

<https://escholarship.org/uc/item/7n37b73p>

Journal

Small, 19(35)

ISSN

1613-6810

Authors

Hernandez, Victor

Jordan, Robert S

Hill, Ian M

et al.

Publication Date

2023-08-01

DOI

10.1002/smll.202207100

Peer reviewed

Deformation Rate-Adaptive Conducting Polymers and Composites

Victor Hernandez, Robert S. Jordan, Ian M. Hill, Bohao Xu, Chenxi Zhai, Di Wu, Hansong Lee, John Misiaszek, Kiana Shirzad, Miguel F. Martinez, Ahmet Kusoglu, Jingjie Yeo, and Yue Wang*

Materials are more easily damaged during accidents that involve rapid deformation. Here, a design strategy is described for electronic materials comprised of conducting polymers that defies this orthodox property, making their extensibility and toughness dynamically adaptive to deformation rates. This counterintuitive property is achieved through a morphology of interconnected nanoscopic core–shell micelles, where the chemical interactions are stronger within the shells than the cores. As a result, the interlinked shells retain material integrity under strain, while the rate of dissociation of the cores controls the extent of micelle elongation, which is a process that adapts to deformation rates. A prototype based on polyaniline shows a 7.5-fold increase in ultimate elongation and a 163-fold increase in toughness when deformed at increasing rates from 2.5 to 10 000% min⁻¹. This concept can be generalized to other conducting polymers and highly conductive composites to create “self-protective” soft electronic materials with enhanced durability under dynamic movement or deformation.

electronics are exposed on the surface of the human body and can easily deform under varying strain rates due to the dynamic movement of bodies.^[1–3] Therefore, it is crucial to address the inverse relationship between deformation rates and material integrity in order to improve the durability of these devices.

Among the many soft electronic materials,^[4–10] organic materials such as conjugated, conducting polymers have attracted significant interest due to their excellent processibility, flexibility, and cost effectiveness. They are commonly employed in energy storage devices,^[11–14] electronics,^[15–19] photocatalysis,^[20,21] coatings,^[22,23] and clarifying agents for water treatment.^[24,25] However, like other thermoplastic polymers, conducting polymers become increasingly susceptible to damage as deformation rates increase.

This is due to their intrinsic viscoelasticity, a classical rate-dependent behavior common to virtually all thermoplastic polymers.^[26–28] The viscoelastic stress relaxation of thermoplastics under loading arises principally from polymer chain rearrangement, disentanglement, and scission.^[28,29] At low strain rates, entangled polymer chains have sufficient time to rearrange and slip under strain, allowing the material to deform and elongate without breaking. However, at high strain rates, this process is hindered due to the shorter timescale, resulting in lower fracture strain, poorer material toughness (i.e., area under the stress–strain curve), and premature failure (**Figure 1a**; and **Figure S1**, Supporting Information).^[28,29] Strategies based on supramolecular bonding or sacrificial networks have been developed to create very tough and/or highly extensible materials, but they still possess this classical inverse relationship between strain rate and material's fracture strain and toughness.^[30–35] As a result, increasing fractions of their impressive mechanical characteristics are sacrificed with increasing rates of deformation. A select few material systems, including polymer nanocomposites^[36–39] and polyurea-based polymers,^[40] exhibit a unique property of defying the classical strain rate trend in the ballistic rates range (e.g., > 10⁶% min⁻¹). Although these rates make them important materials for blast-mitigation applications, they are not directly useful for soft electronics applications, which operate in the range of physiological movements. This classical rate-dependent property of thermoplastics

1. Introduction


Electronics are susceptible to damage from accidents involving rapid impacts or excessive forces. While devices like laptops and smartphones are often protected with cases and careful handling, this may not be feasible for emerging generations of soft electronics such as wearable or on-skin devices. These

V. Hernandez, R. S. Jordan, I. M. Hill, B. Xu, D. Wu, H. Lee, J. Misiaszek, K. Shirzad, Y. Wang
Department of Materials Science and Engineering
University of California, Merced
Merced, CA 95343, USA
E-mail: yuewang@ucmerced.edu

C. Zhai, J. Yeo
Sibley School of Mechanical and Aerospace Engineering
Cornell University
Ithaca, NY 14850, USA

M. F. Martinez, Y. Wang
Department of Chemistry and Biochemistry
University of California, Merced
Merced, CA 95343, USA

A. Kusoglu
Lawrence Berkeley National Lab
Berkeley, CA 94720, USA

 The ORCID identification number(s) for the author(s) of this article can be found under <https://doi.org/10.1002/smll.202207100>.

DOI: 10.1002/smll.202207100

is seldom discussed in the field of organic soft electronics. Most studies only characterize the materials at a fixed, low strain rate (e.g., 30% min⁻¹), which does not reflect the dynamic conditions in which soft electronics are used.

We aimed to free conducting polymers from this restrictive mechanical behavior and asked if it is possible to develop a counterintuitive property where the extensibility and toughness of the material increase with increasing rates of deformation (Figure 1b). This means the electronic materials would be “appropriately extensible and tough” for the instantaneous condition they are experiencing—moderately extensible and tough under normal use, but have enhanced extensibility and toughness during rapid deformation or impact, allowing the resulting electronics to “self-protect” from damage. Our inspiration came from an unlikely source: corn starch slurry, a shear-thickening fluid (STF).^[41–43] We can easily run our hands through corn starch slurry or other STF, but they become hard and resistant to penetration if we hit the surface rapidly. That is because beyond a critical shear rate, the viscosity of STF increases with increasing shear rates, making them dynamically adaptive to impact strength (Figure S2b, Supporting Information).

Inspired by such solution behavior, we aimed to create similar “self-protective” properties in solid-state conducting polymers and soft electronics for their extensibility and toughness to adapt to deformation rates. Here, we present a general material design strategy that realizes this goal, first for conducting polymers, then extended to conducting polymer-containing composites while retaining their high electrical conductivity. This property is achieved through an interplay of deformation mechanisms across multiple length scales with disparate chemical interactions. The change in intermolecular interactions regulates the deformation of the interconnected nanoscopic structures, which in turn dictates the macroscopic mechanical properties. The resulting materials are also self-healing and 3D printable, which are additional attractive features for next-generation, personalized soft electronics.

2. Results and Discussion

2.1. Material Design Principles

One important category of STF is associative polymer solutions,^[44–46] which we hypothesize can serve as a design inspiration for our mission due to their polymeric nature. These polymers typically have solvophobic side-chains or blocks that cause the polymers to aggregate into clusters of micelles in solution (Figure S2a, Supporting Information).^[45–48] At a sufficiently high shear rate, some of the solvophobic interaction in the micelles’ cores are overcome by work done through shear force, leading to chain stretching. The exposed solvophobic moieties on the stretched chains can then form intermicelle crosslinking sites through solvophobic interactions, strengthening the network, leading to an increase in viscosity (Figure S2a,b, Supporting Information).

One thoroughly-investigated associative polymer solution is based on hydrophobically-modified poly(2-acrylamido-2-methyl-1-propanesulfonate).^[45,46] We hypothesized that its unmodified, acidic version, poly(2-acrylamido-2-methyl-1-propanesulfonic

acid) (PAMPSA) can be a possible candidate for creating adaptive behavior in solid conducting polymers because 1) the negatively charged, strongly acidic sulfonic acid group on the side chains is a good dopant for conducting polymers, and 2) a hydrophobic modification of PAMPSA can be created with the polymerization and electrostatic complexation of low molecular weight, positively charged conducting polymers, which are not water soluble.^[49] Polyaniline (PANI) is chosen as the model conducting polymer due to the ease of synthesis and well-characterized properties.^[50] Considering that PANI typically has molecular weight of <20 kDa,^[51] a high molecular weight PAMPSA (~2000 kDa) is selected to promote the formation of discrete hydrophobic PANI:PAMPSA blocks along a hydrophilic PAMPSA chain (Figure 1c,e).^[52] In order to create high stretchability without compromising electrical conductivity, we incorporated 27 wt% (31 mol%) of 1-propanesulfonic acid (PSA) (Figure 1d) as a plasticizing dopant: the sulfonic acid group dopes PANI to enhance conductivity, while the hydrocarbon tail plasticizes the PANI:PAMPSA complex by increasing the free volume between polymer chains (Figure S8a, Supporting Information).

Processing this complex in water drives the association of the hydrophobic PANI:PAMPSA blocks, leading to micelle formation with a PANI:PAMPSA core surrounded by a swelled, solvophilic PAMPSA corona.^[53,54] As the dispersion dries, the increase in its concentration brings the micelles into close proximity where PAMPSA chains from adjacent micelle coronas interact and associate (Figure 1e).^[47] Upon complete solvent removal, an interconnected micelle (ICM) morphology is formed, which can be visualized using scanning electron microscopy (SEM) (Figure 1h; and Figure S7, Supporting Information). The micelles have diameters of ~70–90 nm. The infiltrated interfaces between adjacent micelles are physically crosslinked by chain entanglement and noncovalent hydrogen bonds of N–H···O and S=O···H from PAMPSA (Figure 1f). The extensive hydrogen bonding network and the plasticizing effect of PSA render the resulting material highly stretchable and self-healing (Figure 1g), desirable properties for soft electronics.

As the resulting solid films are elongated under strain rates ($\dot{\epsilon}$) between 2.5% and 160% min⁻¹, the elongation at break (ϵ_b) increases from ~167% to ~1200%, a ~7-fold increase (Figure 1i). Coupled with the simultaneously increasing ultimate tensile stress (UTS), characteristic of viscoelastic materials, the material toughness increases by 254-fold, from 0.0073 to 1.86 MJ m⁻³, demonstrating the dynamic rate-adaptive mechanical properties (Figure 1j; and Figure S6, Supporting Information). This behavior is in stark contrast to classical viscoelastic materials where ϵ_b and $\dot{\epsilon}$ have an inverse relationship (Figure 1a; and Figure S1, Supporting Information). We call materials with this composition strain rate-adaptive conducting polymers (StRAP). However, as the strain rate is increased beyond 160% min⁻¹, ϵ_b starts to decrease with increasing $\dot{\epsilon}$, reverting to conventional viscoelastic rate behavior. This trend reversal is analogous to the transition from shear-thickening to shear-thinning in associative polymer solutions at high shear rates when the newly formed inter-micelle crosslinks are disrupted (Figure S2, Supporting Information).

Despite the successful creation of adaptive properties in solid within a certain $\dot{\epsilon}$ range, the electrical conductivity of

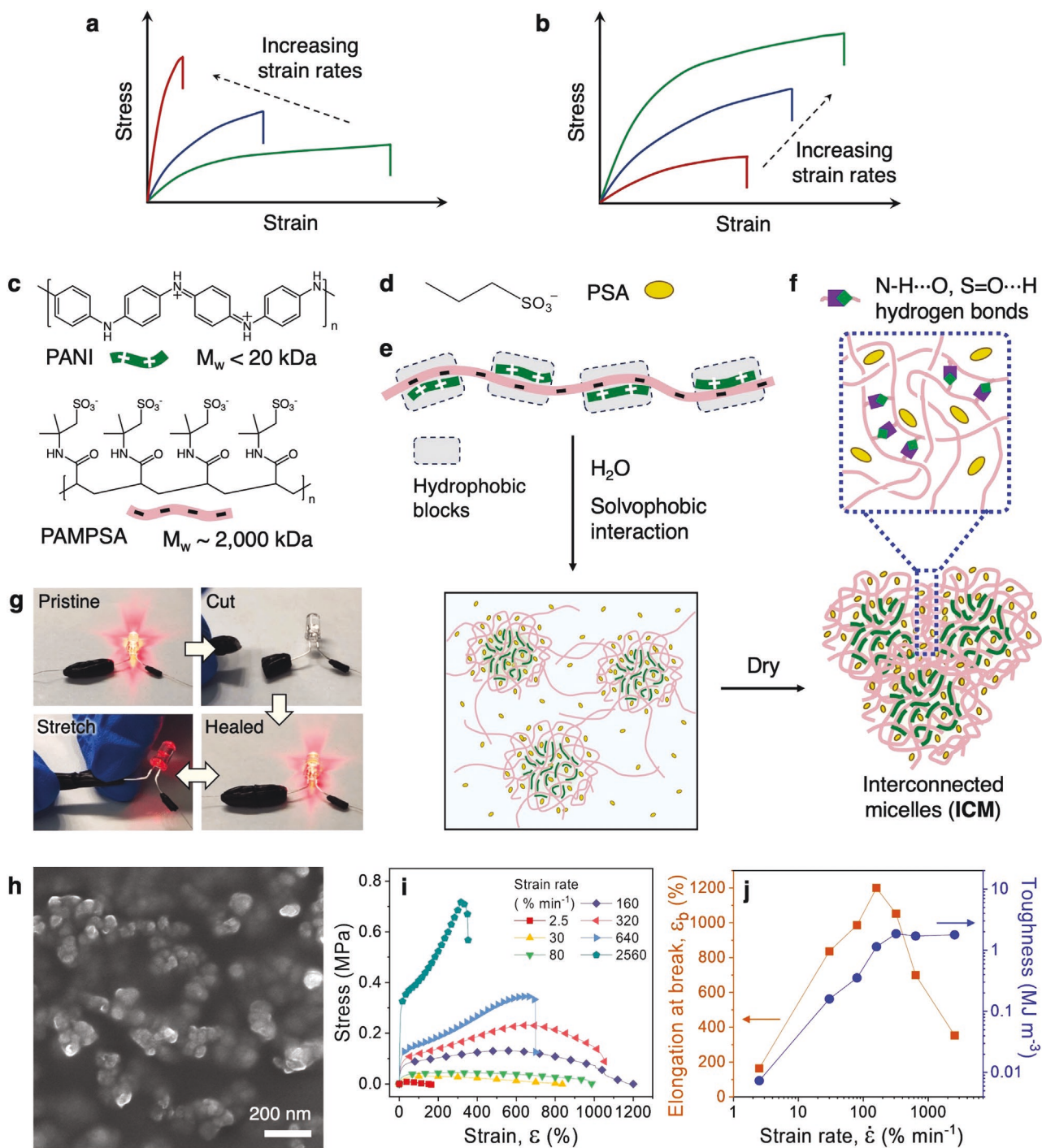


Figure 1. Overview of the strain rate-adaptive conducting polymers (StRAP) material system. a,b) Strain rate behavior of a) conventional thermoplastic polymers and b) deformation rate-adaptive polymers. c) Chemical structures and approximate molecular weights of PANI:PAMPSA. d) Chemical structure of PSA. e) Schematic drawing illustrating the chemical nature of PANI:PAMPSA and the formation process of the interconnected micelle (ICM) morphology in solid-state. f) Schematic illustration of the noncovalent interactions crosslinking the interfaces of the interconnected micelles. g) Photographic series demonstrating the self-healing and conductive properties of StRAP. h) Scanning electron microscope image showing the ICM morphology. i) Stress–strain behavior of StRAP under different strain rates. j) Relationship between strain rate ($\dot{\epsilon}$), elongation at break (ϵ_b), and toughness, extracted from (i).

StRAP is unsatisfactory ($\approx 10^{-3} \text{ S cm}^{-1}$), likely because the PANI-rich conductive cores are isolated from each other by the insulating PAMPSA shells. To circumvent this issue, we

incorporated ≈ 6.7 wt% of the highly conductive Clevis PH1000 poly(3,4-ethylenedioxythiophene):poly(styrene sulfonate) (PEDOT:PSS) into StRAP.^[55] We refer to this conducting

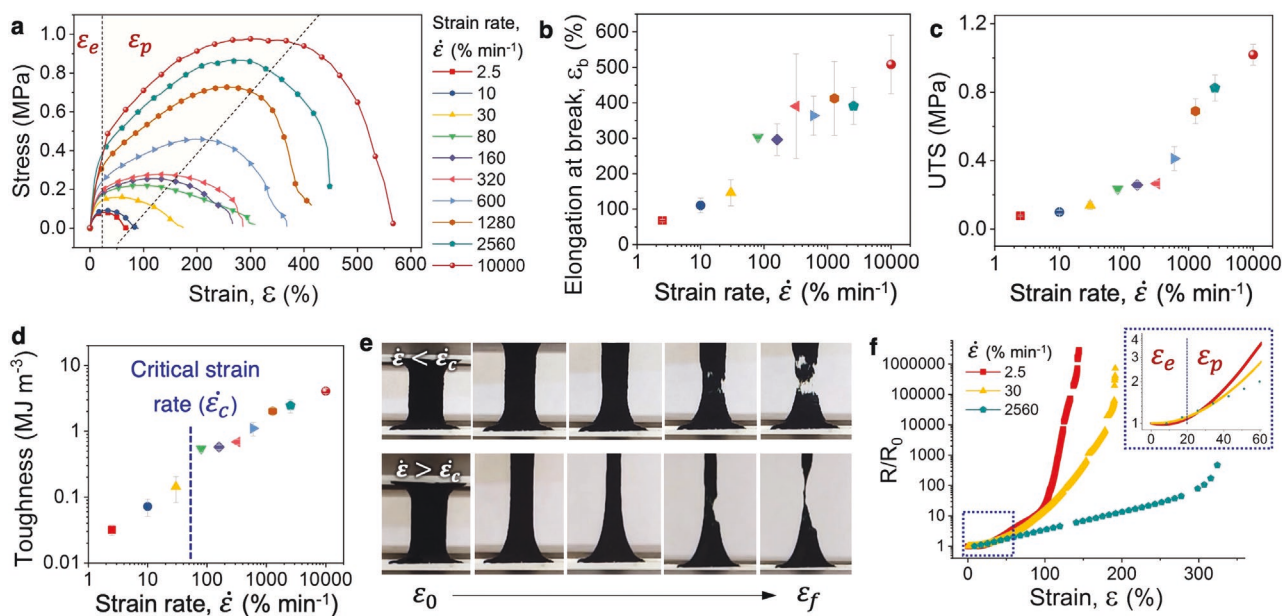


Figure 2. Mechanical and electrical properties of StRAP-P. a) Stress–strain behavior of the polymer blend under various strain rates. ϵ_e and ϵ_p denote elastic and plastic deformation regions, respectively. b–d) Relations between elongation at break (ϵ_b), ultimate tensile stress (UTS), and toughness with strain rates, respectively. e) Photographic series capturing the mechanical failure process of StRAP-P elongated at a strain rate ($\dot{\epsilon}$) below (top) and above (bottom) the critical strain rate ($\dot{\epsilon}_c$), respectively. ϵ_0 and ϵ_f denote initial and final strains, respectively. f) Resistance–strain relations of StRAP-P under different strain rates. The resistance change in the low-strain region is enlarged in the inset.

polymer blend as StRAP-P (a comprehensive list of abbreviations used in this manuscript is provided in Tables S1–S3, Supporting Information). The inclusion of PEDOT:PSS increases the material conductivity to $\approx 100 \text{ S cm}^{-1}$, sufficient for many electronics applications (Figure S9, Supporting Information).^[56] SEM reveals that PEDOT:PSS phase separated from PANI:PAMPSA ICMS to form fiber-rich domains (Figure 3a–c; and Figure S7, Supporting Information). The resulting interconnected PEDOT:PSS network in 3D has likely resulted in significant conductivity enhancement.

The incorporation of PEDOT:PSS also surprisingly extends the adaptive-strain rate range significantly in StRAP, even though the PEDOT:PSS-only counterpart does not display adaptive behavior (Figure S10, Supporting Information). The ϵ_b and UTS of StRAP-P consistently increase with increasing $\dot{\epsilon}$, tested until $10000\% \text{ min}^{-1}$, the maximum of our universal testing machine (Figure 2a). No trend reversal is observed. As $\dot{\epsilon}$ increases from 2.5 to $10\,000\% \text{ min}^{-1}$, ϵ_b increases by over 7-fold, from $\approx 68\%$ to 510% (Figure 2b). Combined with the consistently increasing UTS, the material toughness displays an extraordinary, over two orders of magnitude (163-fold) increase, from 0.025 to 4.1 MJ m^{-3} , within this $\dot{\epsilon}$ -rate range, illustrating its remarkable dynamical adaptability (Figure 2d).

2.2. Mechanistic Investigation

The mechanical characteristics of StRAP-P suggest its deformation mechanism is different from typical viscoelastic materials. We set out to answer two intertwined questions: 1) What is the origin of the strain rate-adaptive behavior in StRAP-P and 2) Why does PEDOT:PSS extend the strain rate range of the adaptive

behavior? We separately investigate the nanoscopic morphological changes, energy dissipation pathways, and function of PEDOT:PSS in relation to strain rates, which collectively reveal the unique multiscale deformation mechanism of StRAP-P.

From the stress–strain curves (Figure 2a), a negative-to-positive slope transition occurs in the plastic deformation region (ϵ_p) with increasing $\dot{\epsilon}$. This transition indicates a change from strain-softening to strain-hardening deformation mechanisms. We define the strain rate at which this transition occurs as the critical strain rate, $\dot{\epsilon}_c$, which for StRAP-P is at $\approx 47\% \text{ min}^{-1}$ (Figure S11, Supporting Information). This transition can also be observed visually. When strained below $\dot{\epsilon}_c$, the film disintegrates at multiple junctions (Figure 2e, top), corroborating strain-softening associated with the loss of micelle connectivity. Conversely, straining the StRAP-P above $\dot{\epsilon}_c$ produces a deformation process characterized by a continuous thinning of the cross-sectional area of the film until a final break occurs (Figure 2e, bottom), consistent with strain-hardening, suggesting that the ICM interfaces retain their integrity to a high strain.

Further support for this mechanistic transition at $\dot{\epsilon}_c$ is observed in the normalized resistance (R/R_0) change under tensile loading (Figure 2f). Little difference in R/R_0 is observable in the elastic deformation region (ϵ_e) among all strain rates. However, in the ϵ_p region, films stretched at $\dot{\epsilon} > \dot{\epsilon}_c$ (e.g., $2560\% \text{ min}^{-1}$) show much smaller resistance changes compared to when they are stretched at $\dot{\epsilon} < \dot{\epsilon}_c$ (e.g., $30\% \text{ min}^{-1}$). This further suggests that polymer chains and/or domains retain much better connectivity at $\dot{\epsilon} > \dot{\epsilon}_c$.

The difference in the deformation mechanism is additionally reflected by the material's cycling stability. When StRAP-P films are loaded cyclically to 50% strain at 30 and $2560\% \text{ min}^{-1}$ ($\dot{\epsilon} < \dot{\epsilon}_c$ versus $\dot{\epsilon} > \dot{\epsilon}_c$, respectively)

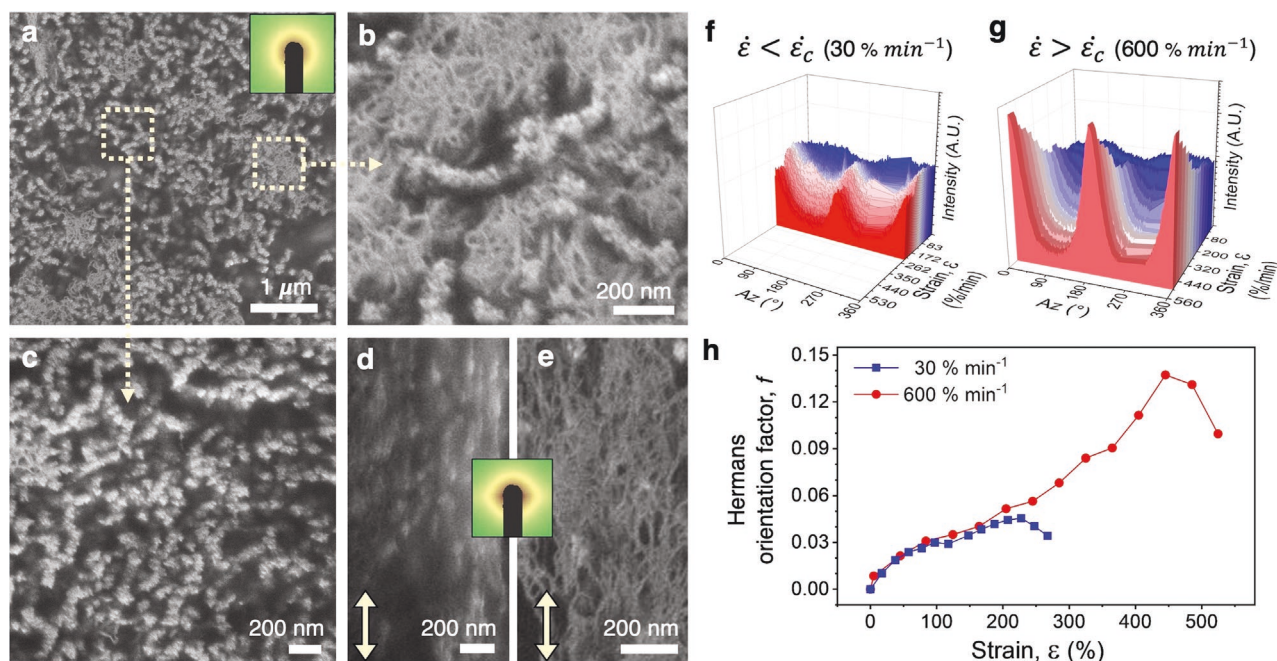


Figure 3. Mechanistic investigation of the StRAP-P deformation mechanism at the nanoscopic scale. a) SEM image showing the morphology of StRAP-P. Morphologies of the fiber-rich and ICM-rich domains in (a) are enlarged in (b) and (c), respectively. Inset in (a) is the 2D SAXS scattering pattern of the film. The morphological changes of the ICM-rich and fiber-rich areas under $\approx 250\%$ elongation at $600\% \text{ min}^{-1}$ ($\dot{\epsilon} > \dot{\epsilon}_c$) can be observed in SEM images shown in (d) and (e), respectively. Stretching direction is indicated by the arrows. The inset between (d) and (e) is the 2D SAXS scattering pattern of the film under the same strain. f,g) Stacked azimuthal angle plots under increasing strain, extracted from the 2D SAXS scattering patterns, for strain rates of $30\% \text{ min}^{-1}$ ($\dot{\epsilon} < \dot{\epsilon}_c$) and $600\% \text{ min}^{-1}$ ($\dot{\epsilon} > \dot{\epsilon}_c$), respectively. h) Hermans orientation factor extracted from the SAXS scattering data at various strains when deformed at $30\% \text{ min}^{-1}$ ($\dot{\epsilon} < \dot{\epsilon}_c$) and $600\% \text{ min}^{-1}$ ($\dot{\epsilon} > \dot{\epsilon}_c$).

for 1000 repetitions, films display significantly higher mechanical and electrical stability at $\dot{\epsilon} > \dot{\epsilon}_c$ than $\dot{\epsilon} < \dot{\epsilon}_c$ (Figures S14 and S15, Supporting Information). At $\dot{\epsilon} < \dot{\epsilon}_c$, the maximum stress and hysteresis of the film decrease rapidly with each additional loading–unloading cycle (Figure S14a–c, Supporting Information), indicating increasing interfacial disintegration of ICMs under repeated cycling. The films consistently fail after ≈ 600 cycles at this strain rate. Conversely, at $\dot{\epsilon} > \dot{\epsilon}_c$, a sizable decrease in maximum stress and hysteresis is observed during the first three cycles of stretching. Afterward, the stress–strain curves show only a minor reduction in hysteresis through the end of the 1000th cycle (Figure S14d–f, Supporting Information), indicating the preservation of ICM interfacial connectivity.

This difference in cycling stability is also reflected in the normalized electrical resistance over cycles. As shown in Figure S15a,b (Supporting Information), at $30\% \text{ min}^{-1}$ ($\dot{\epsilon} < \dot{\epsilon}_c$), the normalized resistance along the loading direction increases consistently up to 4.3-fold within the first ≈ 30 cycles due to interfacial disintegration of the micelles. On the contrary, at $2560\% \text{ min}^{-1}$ ($\dot{\epsilon} > \dot{\epsilon}_c$), the resistance only increases by ≈ 1.9 -fold in the first 8 cycles because the film's overall integrity was preserved through the strain-hardening (Figure S15c,d, Supporting Information).

2.3. Deformation Mechanism at Nanoscale

To understand the deformation mechanism at the nanoscopic micelle level, we employed in situ synchrotron small-angle

X-ray scattering (SAXS) under uniaxial tensile loading at $\dot{\epsilon} < \dot{\epsilon}_c$ ($30\% \text{ min}^{-1}$) and $\dot{\epsilon} > \dot{\epsilon}_c$ ($600\% \text{ min}^{-1}$). In the unstrained state, the film exhibits an isotropic scattering pattern (Figure 3a inset; and Figure S16, Supporting Information). The extracted 1D profiles show a weak, broad shoulder peak at $\approx 0.0073 \text{ \AA}^{-1}$ ($\approx 86 \text{ nm}$), which corresponds to the average ICM sizes (Figure S17, Supporting Information). Under uniaxial elongation (tensile direction is parallel to z-axis), the ring evolves into an elliptical pattern under both $\dot{\epsilon} < \dot{\epsilon}_c$ and $\dot{\epsilon} > \dot{\epsilon}_c$, reflecting an orientation developing along the stretching direction (inset to Figure 3d,e; and Figure S16, Supporting Information).^[57,58] Stacked plots of intensities as a function of the azimuthal angle (A_z) for scattering patterns at various strains illustrate that the extent of micelle orientation and elongation increases with increasing strains at both $\dot{\epsilon} < \dot{\epsilon}_c$ and $\dot{\epsilon} > \dot{\epsilon}_c$, but to a much greater degree at $\dot{\epsilon} > \dot{\epsilon}_c$ (Figure 3f,g). ICM alignment and elongation at $\dot{\epsilon} > \dot{\epsilon}_c$ can be visualized directly under SEM on transfer-printed films immobilized under tension (Figure 3d). PEDOT:PSS fiber bundles also align along the tensile direction (Figure 3e), indicating that they may also have contributed to the scattering anisotropy. Given that PEDOT:PSS only constitutes $< 7\%$ of the material, we expect its contribution to be minor.

This micelle domain anisotropy is further quantified by the Hermans orientation factor (f)^[59]

$$f = \frac{3(\cos^2 \varphi) - 1}{2}, \quad (\cos^2 \varphi) = \frac{\int_0^{\pi/2} I(\varphi) \cos^2 \varphi \sin \varphi \, d\varphi}{\int_0^{\pi/2} I(\varphi) \sin \varphi \, d\varphi} \quad (1)$$

where f is Hermans orientation factor varying from 0 to 1. Structural isotropy is indicated by $f=0$, whereas $f=1$ indicates completely anisotropic alignment perpendicular to the strain direction. I is intensity, and φ is the azimuthal angle.^[60,61] The f is nearly identical in the lower strain region for $\dot{\epsilon} < \dot{\epsilon}_c$ and $\dot{\epsilon} > \dot{\epsilon}_c$, but starts to diverge at around 80% strain (Figure 3h). Beyond that, the domain anisotropy increases faster at $\dot{\epsilon} > \dot{\epsilon}_c$ than $\dot{\epsilon} < \dot{\epsilon}_c$. At $\dot{\epsilon} < \dot{\epsilon}_c$, the anisotropy starts decreasing at around 200% strain, suggesting relaxation of micelles, likely due to material failure through micelle dissociation (Figure 2e, top). Conversely, at $\dot{\epsilon} > \dot{\epsilon}_c$, the domain anisotropy continues to increase until over 400% strain. These results indicate that ICMs retain connection better during elongating at $\dot{\epsilon} > \dot{\epsilon}_c$ than $\dot{\epsilon} < \dot{\epsilon}_c$, supporting the mechanistic transition from strain-softening to strain-hardening at $\dot{\epsilon}_c$.

2.4. Energy Dissipation Mechanism

At $\dot{\epsilon} < \dot{\epsilon}_c$, energy from elongation is dissipated through ICM interfacial dissociation. At $\dot{\epsilon} > \dot{\epsilon}_c$, however, the intact interfaces until high strain suggests the presence of a different energy-dissipation pathway that dynamically scales with $\dot{\epsilon}$, leading to adaptive ϵ_b and toughness. In situ tensile-wide-angle X-ray scattering (WAXS) is used to study the responsible intermolecular events during straining. The peak that shows noticeable differences at $\dot{\epsilon} < \dot{\epsilon}_c$ versus $\dot{\epsilon} > \dot{\epsilon}_c$ centers at $\approx 0.52 \text{ \AA}^{-1}$ ($d \approx 12 \text{ \AA}$), which can be assigned to the lamella stacking between alternating PANI-PAMPSA electrostatic complexes ($d_{\text{PANI-PAMPSA}}$),^[62,63] which forms the core of the ICMs (Figure 4b–e; and Figure S19e, Supporting Information). At $\dot{\epsilon} < \dot{\epsilon}_c$, the $d_{\text{PANI-PAMPSA}}$ scattering peaks from all strain values, regardless of orientation, mostly overlap, indicating little change in lamella spacing or orientation with micelle elongation (Figure 4b,c). However, at $\dot{\epsilon} > \dot{\epsilon}_c$, the $d_{\text{PANI-PAMPSA}}$ peak intensity along q_x decreases with increasing strain, and the peak shifts from ≈ 0.52 to $\approx 0.46 \text{ \AA}^{-1}$ ($d \approx 12\text{--}13.7 \text{ \AA}$) (Figure 4d). This suggests that at $\dot{\epsilon} > \dot{\epsilon}_c$, there is a decrease in PANI-PAMPSA lamella periodicity along the stretching direction with increasing strain, implying the micelle cores are dissociating into smaller fragments (Figure 4a). This decrease in $d_{\text{PANI-PAMPSA}}$ peak intensity along q_x is accompanied by a slight increase in $d_{\text{PANI-PAMPSA}}$ peak intensity along q_z (Figure 4e).

To uncover the origin of the directional preference of core fractures and the rise in q_z lamella peak intensity, we conduct coarse-grained molecular dynamics (CGMD) simulation to reveal intermolecular events during rate-dependent deformation. Equilibrating the StRAP composition generates a randomly-oriented lamella structure between PANI and PAMPSA. Elongation of the bulk material places the ICM cores under shear (Figure S21a, Supporting Information). In the simulation, when directional shear is applied, the PANI-PAMPSA lamella align along the shear direction, leading to a temporary increase in PANI-PAMPSA interfaces that can dissociate under further shear stress. This gradual dissociation leads to an increased aspect ratio of the lamella cluster (Figure 4f). This process is shown to generate both increased ultimate stress and ϵ_b , such that the simulation replicates the experimental trends of adaptive strain rate behavior (Figure 1g,h; and Figure S21c–f, Supporting Information).

Considering that only the lamella, but not the clusters/crystallites of ordered PANI-PAMPSA stacks, is computationally modeled due to the inherent spatiotemporal limits in CGMD, we conjecture that the PANI:PAMPSA crystallites orient along the shear/elongation direction, leading the constituting PANI-PAMPSA lamella to orient either parallel or perpendicular to the shear/elongation direction (Figure 4g). This would lead to an increase in lamella peak intensity along both q_x and q_z , but it is only observed along q_z (Figure 4e). The decrease in q_x peak intensity and spacing (i.e., increasing in d_x spacing) suggests that the lamella parallel to the shear/elongation direction is being preferentially dissociated, likely through the breaking-slipping-exchange of electrostatic interactions (Figure 4f). This process dissipates energy while releasing “hidden length”^[64,65] through the increasing aspect ratio of the deforming lamella, allowing micelles to elongate. Continued strain leads more lamella to dissociate into smaller pieces, decreasing the crosslinking density of the micelle cores, providing the interconnected shells with additional freedom to elongate, resulting in higher ϵ_b . A higher strain rate translates to more mechanical work done and more available energy to dissociate cores into larger numbers of fragments, making ϵ_b , UTS, and toughness dynamically adaptive to deformation rates. On the other hand, the dissociation of PANI-PAMPSA lamella oriented perpendicular to shear direction (corresponding to the q_z peak) is unfavorable because significant energy is required to break an entire array of bonds simultaneously (Figure S20b, Supporting Information), leading to the preferential directionality in the fragmentation of PANI:PAMPSA crystallites.

2.5. Function of PEDOT:PSS

The extended adaptive-strain rate range in StRAP-P compared to StRAP can be attributed to the fiber-reinforcement effect of the PEDOT:PSS nanofiber-bundles (Figure 3b). The energy required for fiber pull-out, fiber debonding from the matrix, and fiber breakage are all effective additional mechanisms for energy dissipation, leading to enhanced toughness.^[66–68] In particular, fiber pull-out and debonding are rate-dependent properties:^[69] lower $\dot{\epsilon}$ provides more time for such decoupling, leading materials to lose connection more easily, whereas faster $\dot{\epsilon}$ stifles such decoupling, diverting energy dissipation through core defragmentation. Furthermore, in StRAP-P, the sulfonic acid groups on PSS from the fibers can hydrogen bond to the sulfonic acid and amide groups on PAMPSA from the ICM shells. The energy associated with faster $\dot{\epsilon}$ can also be dissipated through the temporary, reversible decoupling–recoupling of these hydrogen bonds, preventing or minimizing energy dissipation through fiber or material breakage. In fact, minor strain rate-adaptive behavior ($\approx 2\%$ increase in ϵ_b as $\dot{\epsilon}$ increases from 6 to 2400 000% min^{-1}) has been observed in certain glass fiber-reinforced thermoplastics.^[70] Such fiber-reinforcement effects likely interact synergistically with the ICM deformation mechanism, leading to the remarkable increase in ϵ_b and material toughness across a broad $\dot{\epsilon}$ range (Figure 2a–d).

To confirm this hypothesis, we replaced PEDOT:PSS fiber bundles with hydroxylated multiwalled carbon nanotubes (MWCNT), which can interact with PANI:PAMPSA through

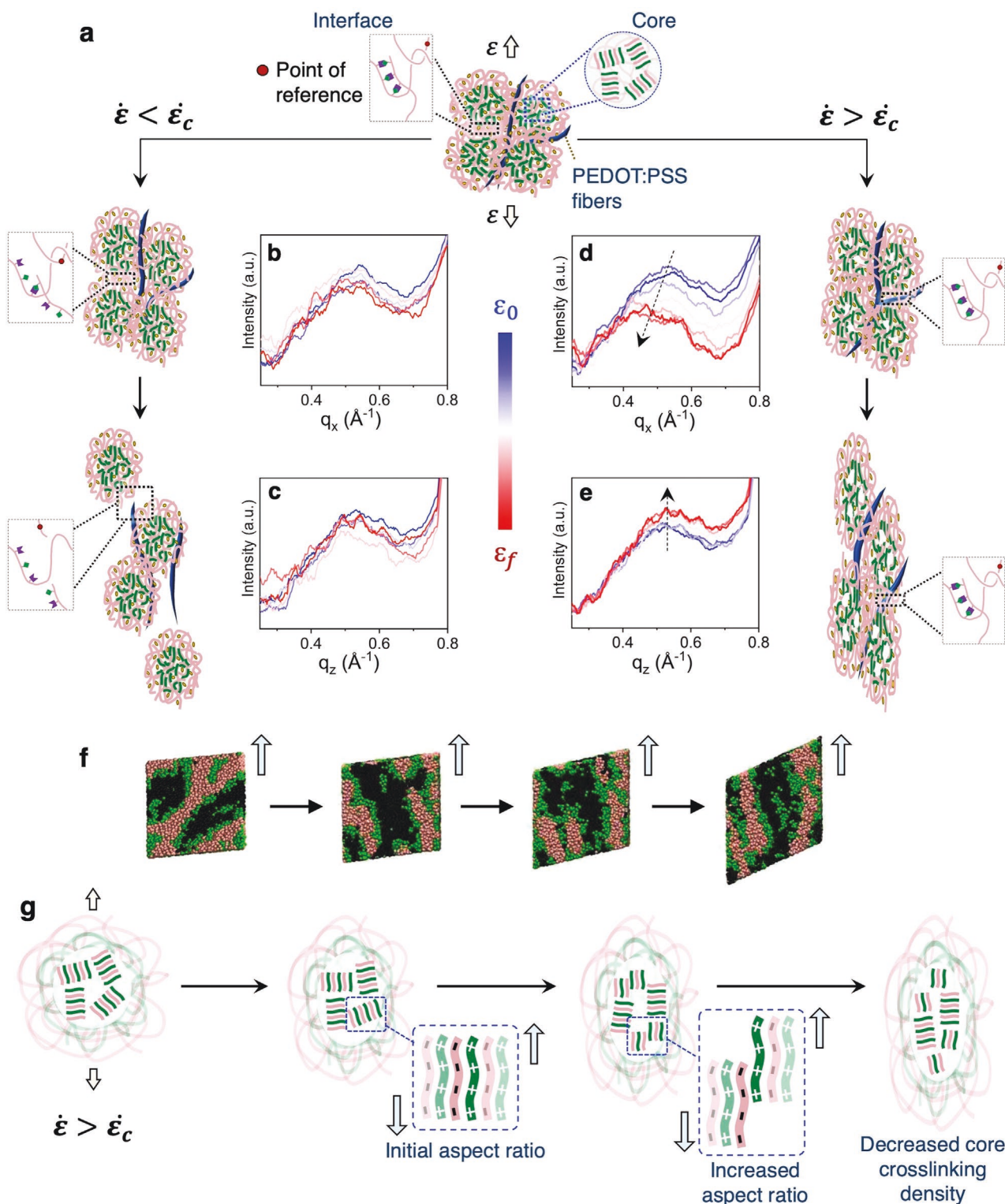


Figure 4. a) Schematic drawing illustrating the different deformation mechanisms at the nanoscale domain and angstrom intermolecular levels when StRAP-P is deformed at $\dot{\epsilon} < \dot{\epsilon}_c$ versus $\dot{\epsilon} > \dot{\epsilon}_c$. The deformation mechanism within the micelle cores is derived from the in situ tensile-WAXS data, shown in (b–e), collected at strain rates below $\dot{\epsilon}_c$ (b,c) and above $\dot{\epsilon}_c$ (d,e). q_x and q_z are directions perpendicular and parallel to the stretching direction, respectively. The $\approx 0.52 \text{ \AA}^{-1}$ ($d \approx 12 \text{ \AA}$) peak corresponds to the $d_{\text{PANI-PAMPSA}}$ lamella stacking distance. ϵ_0, ϵ_0 , and ϵ_f on the legend represents initial and final/fracture strain, respectively. f) MD simulation of the deformation process of the lamella core under shear. g) Schematic diagram showing the ICM core dissociation mechanism.

electrostatic and hydrogen bonding interactions similar to PEDOT:PSS. A similar extension of adaptive strain rate range compared to the StRAP (Figure 1i,j) is obtained, where ϵ_b consistently increases from ≈ 640 to 1320% as $\dot{\epsilon}$ is increased from 30 to 10000% min^{-1} (Figures S23 and S24, Supporting Information). These results not only confirm the function of PEDOT:PSS, but also reveal that fillers that are more conductive than PEDOT:PSS can potentially be used to enhance both electrical conductivity and adaptive strain rate range.

2.6. Multiscale Deformation Mechanism

Collectively, our mechanistic investigations depict the following deformation mechanism for StRAP-P (Figure 4a). The StRAP-P films with the ICM morphology are physically crosslinked both at the adjacent micelle interfaces and within each micelle core, but through different chemical interactions: chain entanglement and hydrogen bonding at PAMPSA-rich ICM interfaces, and weaker electrostatic interaction within PANI:PAMPSA lamella-rich cores. PEDOT:PSS fibers are also intertwined with ICM interfaces at places. The inter-connectedness of ICM interfaces determines the integrity of the bulk material, whereas the crosslinking density within ICM cores regulates the degree of micelle deformation. Under strain, micelles can elongate along the tensile direction to a certain degree. Beyond this extent, the material transitions to deform through one of the two competing mechanisms: 1) through classical viscoelastic chain relaxation at inter-ICM and ICM-PEDOT:PSS fiber interfaces, or 2) through dissociation of the micelle cores into smaller fragments, reducing the crosslinking density within micelles, hence increasing the degree of freedom for ICMs to elongate. At $\dot{\epsilon} < \dot{\epsilon}_c$, deformation through pathway 1) is preferred because there is sufficient time for chain rearrangement and hydrogen bond dissociation,^[71] leaving the ICM cores mostly intact (Figure 4a, left). The PEDOT:PSS fibers also have time to disentangle or debond from the PANI:PAMPSA matrix. This pathway leads the micelles to lose connection and fibers to pull out, resulting in strain-softening and film disintegration. Conversely, at $\dot{\epsilon} > \dot{\epsilon}_c$, pathway (2) is preferred because the deformation rate does not provide sufficient time for significant chain rearrangement and hydrogen bond dissociation at inter-ICM or ICM-PEDOT:PSS interfaces. This normally causes energy dissipation through bond scission of the polymer backbones, leading to lower ϵ_b and premature material failure. However, core-fracturing provides an alternative pathway for energy dissipation, and the associated lowering of the core's crosslinking density provides an enhanced degree of freedom for the interconnected shells to elongate (Figure 4a, right). The rate-adaptive nature of the core fracturing process makes the material's ϵ_b and toughness dynamically adaptive. Even when certain ICMs lose contact, the PEDOT:PSS fibers can bridge the gap, retaining material integrity (Figure 4a, right). The $\dot{\epsilon}$ at which pathway (2) out-competes pathway (1) is the $\dot{\epsilon}_c$.

It should be noted that the strategic arrangement of the various types of interactions and mechanisms across multiple length scales has led to the unusual rate-adaptive extensibility and toughness in our materials.^[72–75] Incorporating individual constituents in isolation is insufficient to overcome

the viscoelastic strain rate behavior. For example, the inclusion of dynamic bonds, either a single type or multiple types with different bond strengths and dissociation time scales, can make the materials less rate-dependent, but they still generally exhibit the classical inverse relationship between deformation rates and elongation at break.^[32,33,34] That is because even though dynamic bonds can regulate the deformation timescale, they are anchored on the polymer backbone, which deforms through viscoelastic stress relaxation mechanisms under strain. For similar reasons, the isolated presence of sacrificial bonds or moieties, such as those in double network hydrogels, can effectively toughen the material, but does not influence the viscoelastic strain rate behavior significantly.^[64,71] The brittle network fractures to absorb energy, resulting in high material toughness. However, the extensibility of the bulk material is offered by the ductile network, and its elongation is again controlled by the viscoelastic stress relaxation of the constituting polymer chains. In terms of fiber-reinforcement effect, its function is mostly to strengthen the material, but occasionally can also provide minor rate-adaptive properties (as discussed under the “Function of PEDOT:PSS” section) albeit not to a significant degree,^[70] i.e., not comparable to the extent of the adaptive behavior reported in this work. Imbuing different chemical interactions in different nanoscopic domains has led to polyurea and polyurethane with rate-adaptive properties that can only be activated at extremely high, ballistic rates (e.g., at $>3600\,000\% \text{min}^{-1}$), and thus are primarily useful in blast-mitigation applications, but not at physiologically relevant rates under which soft electronics operate.^[40,76] These materials adopt a phase-separated morphology comprised of densely hydrogen-bonded crystalline domains embedded in a soft, extensible hydrocarbon, or ethylene oxide-based matrix. Their adaptive mechanism originates from the dissociation of the high-density hydrogen bonds within the urea- or urethane-based crystalline domains. Collective decoupling of large amounts of ordered hydrogen bonds within these crystalline domains requires a significant amount of energy, i.e., energy from ballistic-rate impacts. In the absence of such events, polyurea and polyurethane simply exhibit the classical viscoelastic strain rate behavior of thermoplastics—since the intermolecular interactions within the soft domains are much weaker than those in the crystalline domains, strain is accommodated through the chain relaxation within the soft domains while the hydrogen-bonded crystalline domains remain intact and simply serve as physical crosslinking sites.

On the other hand, the rate-adaptive properties within physiologically relevant rates of our materials is the result of 1) a strategic combination of different dynamic bonds, sacrificial moieties, and fiber-reinforcement effect at multiple length scales, thereby creating competing deformation pathways; 2) the usage of disparate dynamic bonds to tune the relative strength of the core and shell of the ICMs, rather than relying on viscoelastic stress relaxation to tune the time scale of chain deformation. As a result, our materials deform by the collective elongation of interconnected nanoscopic domains. This is regulated by the rate-adaptive dissociation of weaker noncovalent interactions within the cores, which limits or bypasses the classical viscoelastic stress relaxation of polymer chains.

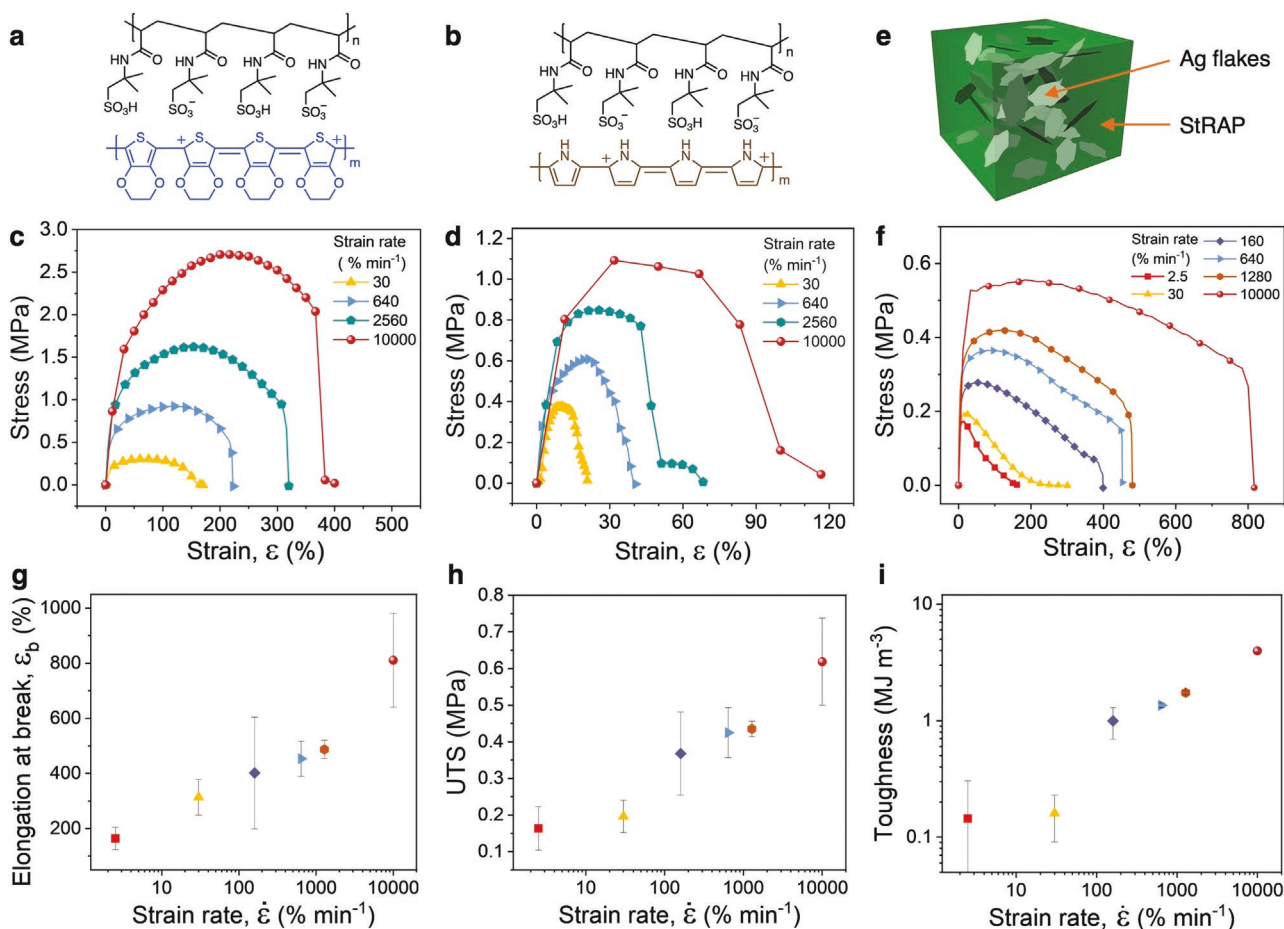


Figure 5. Generality. a,b) Chemical structures and c,d) stress–strain behavior of PEDOT:PAMPSA-P (a,c) and PPy:PAMPSA-P (b,d), respectively. e,f) Schematic diagram and stress–strain behavior, respectively, of an organic–inorganic composite using StRAP as the conductive and stretchable matrix and silver flakes as the highly conductive filler. g–i) Relation between strain rates and elongation at break (g), UTS (h), and toughness (i).

2.7. Generality

We illustrate the generality of this design principle by replicating rate-adaptive behavior in two other benchmark conducting polymers, PEDOT and polypyrrole (PPy), through their complexation with PAMPSA (Figure 5a,b). PEDOT:PSS was added for conductivity enhancement similar to the PANI:PAMPSA system. As $\dot{\epsilon}$ increases from 2.5 to 10000% min⁻¹, the ϵ_b and toughness of PEDOT:PAMPSA-P (-P stands for added PEDOT:PSS) increase from 170% to 434% and 0.7 to 8.0 MJ m⁻³, respectively (Figure 5c), and those for PPy:PAMPSA-P increase from 21% to 117% and 0.04 to 0.87 MJ m⁻³ (Figure 5d), respectively, demonstrating their dynamic adaptability. Hence, we reason that this strategy is broadly applicable to conducting polymers and possibly even other polymers where deformation can be modulated through an ionic network or reversible bonds.

2.8. Mechanically Adaptive Electronic Composites

Conventional stretchable matrices are electrically insulating and do not have adaptive behavior.^[2,77] Our findings on the extension of adaptive $\dot{\epsilon}$ range aided by fiber-reinforcement effect unravel

StRAP's potential as a conductive and mechanically adaptive matrix for other fillers. This hypothesis is validated by a composite comprised of a StRAP matrix and ≈ 25 vol% silver (Ag) flakes, a low-cost filler (Figure 5e).^[77,78] This composite exhibits very high conductivity ($\approx 2890 \pm 150$ S cm⁻¹), likely due to the conductive nature of both matrix and filler. It also retains the strain rate-adaptive behavior of the StRAP matrix (Figure 5f): as $\dot{\epsilon}$ is increased from 2.5 to 10 000% min⁻¹, ϵ_b of the material increases by ≈ 5 -fold, from 160% to 812% (Figure 5g), and the toughness of the material increases by ≈ 29 -fold, from 0.14 to 4 MJ m⁻³ (Figure 5i). The strain-electrical resistance relationship of the composite also resembles that of StRAP-P: the resistance change is smaller across a broader range of strain under high-rate deformation (i.e., 10 000% min⁻¹) than under low-rate deformation (i.e., 2.5% min⁻¹) (Figure S26b, Supporting Information), likely due to the enhanced interfacial connectivity between the ICMs and ICM-Ag flakes at $\dot{\epsilon} > \dot{\epsilon}_c$. These findings show that StRAP has the potential to enhance the mechanical adaptivity of various functional fillers, opening doors to a new class of high-performance, self-protective composites. Similarly, various fillers can be incorporated to potentially tune the mechanical characteristics of StRAP such as stiffness or strength, while retaining its adaptive behavior.

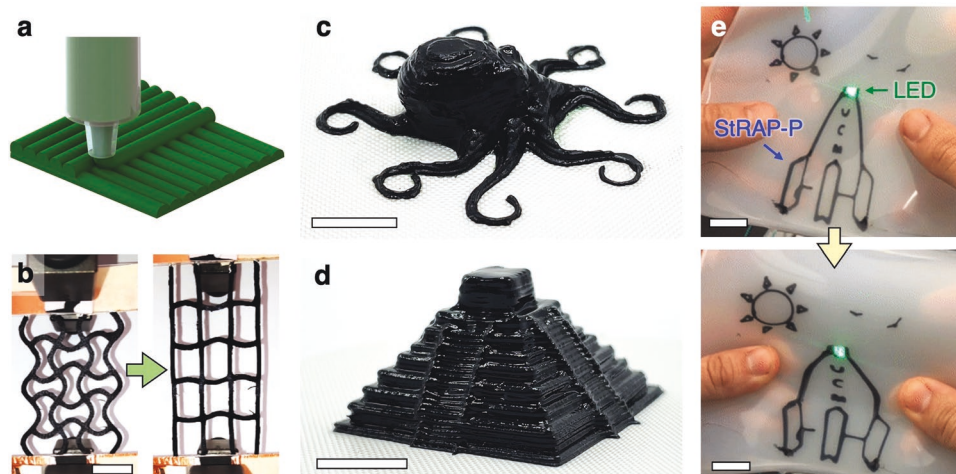


Figure 6. 3D printing of StRAP-P for soft electronics applications. a) Schematic of DIW printing. b) 3D printed auxetic structure in the unstrained (top) and strained (bottom) states. c, d) 3D printed StRAP-P octopus (c) and Mayan pyramid (d). e) 3D printed StRAP-P interconnects for an LED device embedded in silicone in the unstrained state and being stretch at $\approx 10\,000\% \text{ min}^{-1}$. Scale bars = 10 mm.

2.9. 3D Printing

Highly concentrated StRAP-P dispersion (30–35 wt% aqueous paste) can be 3D-printed via direct ink write (DIW)^[79] (Figure 6a; and Figure S27, Supporting Information). Various 3D geometries can be readily created, including auxetic structures, octopus, and Mayan pyramid (Figure 6b–d). StRAP-P can also be printed and embedded into elastomers as interconnects for stretchable electronics such as the proof-of-concept LED device shown in Figure 6e. The light intensity is mostly retained under rapid stretching ($\approx 10\,000\% \text{ min}^{-1}$), revealing StRAP's potential for personalized, 3D, mechanically-adaptive electronics.

3. Conclusions

Using conducting polymers as model systems, we have presented a general strategy to create electronic polymers and composites with a counterintuitive mechanical property: they become more extensible and tougher under more rapid deformation, rendering them “self-protective.” Their electrical and cycling stability are also enhanced under higher rate deformation, potentially enhancing device stability and reliability. These unusual properties are realized through a multiscale design strategy where disparate chemical interactions and nanoscopic structures at different length scales compete to accommodate deformation at different rates. This approach can be generalized to other conducting polymers and conducting polymer-containing composites such as those with silica or ceramic particles for enhancing stiffness, or with gold or silver nanowires for improving conductivity. This adaptive property may also be applicable to other classes of functional polymers by adopting similar chemical and morphological design principles. The 3D-printability of these materials enables their potential application in personalized soft electronics and robotics that can adapt to dynamic movements. Collectively, this new class of polymeric conductors and composites has the potential

to improve device durability and prolong the lifetime of the resulting devices, providing another pathway to decrease the amount of electronic and polymer waste, leading to a more sustainable future.

4. Experimental Section

Materials Preparation: Poly(3,4-ethylenedioxythiophene):poly(styrene sulfonate) (PEDOT:PSS) PH 1000 ($\approx 1 \text{ wt}\%$) was purchased from Clevis. 1-Propanesulfonic acid (95%) was obtained from eNovation Chemicals. Aniline (99.8%), pyrrole ($>98\%$), 3,4-ethylenedioxythiophene (99%), ammonium persulfate (APS, $>98\%$), and Ag flakes ($4\text{--}8 \mu\text{m}$, 90%) were purchased from Fisher Scientific. The 15 wt% aqueous solution of poly(2-acrylamido-2-methyl-1-propanesulfonic acid) (PAMPSA), $M_w = 2\,000\,000 \text{ Da}$, was obtained from Sigma-Aldrich. MWCNT (hydroxylated, $\approx 8\text{--}15 \text{ nm}$ in diameter, $>95\%$) were purchased from ACS Materials. Polymerization and film processing procedures are described in detail in the Supporting Information Sections 1 and 3.

Chemical Characterization: ^1H nuclear magnetic resonance (NMR) spectra were collected on a Bruker 600 MHz NMR and data were processed using Topspin. UV-vis-NIR spectra were collected on a Shimadzu UV-3600 Plus using drop casted films on quartz slides.

Electrical Characterization: A Keithley 2460 SMU SourceMeter was used to measure the electrical properties of materials. Four-point resistance measurements were carried out on drop casted thin films dried from a diluted StRAP dispersion on glass slides (film thickness $\approx 4\text{--}6 \mu\text{m}$). Silver paste (TedPella Leitsilber 200) electrodes were applied to the films and annealed at $130 \text{ }^\circ\text{C}$ for 10 min before measurements. Conductivity was obtained by using equation $\sigma = \frac{L}{A \cdot \Omega}$, where σ is conductivity, L is length, A is cross-sectional area, and Ω is resistance. The film thickness was measured using a Bruker DektakXT profilometer.

Mechanical Characterization: Stress-strain and cyclic stability of freestanding films ($\approx 700 \mu\text{m}$ thick) were obtained using an Instron 3369 universal testing machine with a 100 N load cell. The clamps of the tensometer were wrapped in insulating tapes. In situ resistance-tensile measurements were obtained by adding a piece of copper conductive tape in-between the clamp sections of the tensometer and the sample (Figure S13, Supporting Information). Silver paste adhesive was applied between Cu tape and sample interface to ensure intimate electrical contact. The resistance and stress-strain data were synchronize using time output. Dynamic mechanical analysis of the films was carried out on a TA Instruments Q800.

Morphological Characterization: Sections of free-standing films were directly adhered to a scanning electron microscope (SEM) sample holder using double-sided carbon tape (TedPella). SEM images were collected on a Zeiss Gemini 500 using secondary electrons and the in-lens detector with an electron high tension voltage of 3 kV at a working distance of 3.4–3.7 mm. Multiple regions within each sample were examined to ensure the representativeness of the images. SEM samples of the stretched films were prepared by depositing and air drying a diluted solution of StRAP-P (≈ 0.016 wt%) on 0.3 mm thick Sylgard 184 dog bone specimens, followed by elongation on the tensometer, and immediately transfer-printed onto a piece of silicon wafer to immobilize the morphology under tension.

Synchrotron X-Ray Scattering: Synchrotron small- and wide-angle X-ray scattering (SAXS and WAXS, respectively) experiments were carried out at Beamline 7.3.3 of the Advance Light Source (ALS), Lawrence Berkeley National Lab (LBNL). SAXS/WAXS spectra under tension were collected in situ using a Linkam tensile stage in transmission geometry at 10 keV. The blade-coated free-standing films (≈ 700 μm thick) were elongated at each programmed rate and the images were collected every 10 s with an exposure time of 2 s. Suitable “blank” exposures were collected for each sample for subsequent background subtraction during data processing. Igor Pro Nikka Irena packages were used to analyze and reduce the 2D spectra to obtain integrated intensity versus scattering wave vector (q) and azimuthal line cuts. These data were then extracted and processed using custom Python codes.

Coarse-Grained (CG) Molecular Dynamic (MD) Simulation: A dissipative particle dynamics (DPD) modeling framework, together with the LAMMPS software, is used to simulate the self-assembly of the charged PAMPSA-PANI-PSA system with electrostatic interactions. Some charges are randomly assigned as zero due to protonation to maintain a charge-neutral system. Electrostatic interactions are modeled using Slater smearing to avoid unstable local charge concentration effects at the mesoscale. Through this coarse-graining scheme, longer time scales can be accessed using a larger time step of 7.5 ps, which is about 4 orders of magnitude larger than the time steps commonly used in conventional all-atomistic (AA) MD. The complete experimental details are summarized in Section 16.3 of the Supporting Information.

Printing: An ≈ 30 – 35 wt% StRAP-P paste was used as the ink for DIW printing, which was performed using a custom-modified Discov3ry/Ultimaker printer for structures in Figure 6b,e, and a BIO X Bioprinter (Cellink) for structures in Figure 6c,d. The ink was homogenized and degassed using a Thinky AR-100 planetary mixer (4 min mixing and 30 s defoaming). The ink is left to cool to room temperature (≈ 5 min) and subsequently loaded into a luer-lok syringes. Extrusion nozzles with an inner diameter of 564 μm (Subrex, LLC) were used for all prints. PTFE sheets were used as substrates. For the octopus model, a 25 wt% Pluronic F-127 hydrogel was used as support materials for the overhang portion of the structure. The F-127 support was removed by placing the prints in a fridge for 15 min, which induced a sol-gel transition for F-127, allowing it to flow away.

Supporting Information

Supporting Information is available from the Wiley Online Library or from the author.

Acknowledgements

V.H. and R.S.J. contributed equally to this work. The authors thank Emily Tran for assisting with graphic illustrations, Adrian Giglio for helping with 3D printing, and Israel Alberto, Alan Ramirez, and Jacob Frye for aiding with mechanical and electrical characterization. Y.W. acknowledges support from the U.S. National Science Foundation-CAREER (No. DMR-1945664), Beckman Young Investigator Award from the Arnold and Mabel Beckman Foundation, and the University of California, Merced

startup fund. J.Y. acknowledges support from the U.S. National Science Foundation (Grant No. 2038057), the Cornell University faculty startup fund, and computational resources provided by the NSF ACCESS program under Grant No. TG-BIO210063. A.K. acknowledges funding from the Office of Energy Efficiency and Renewable Energy of the U.S. Department of Energy (DOE) under Contract No. DE-AC02-05CH11231. Synchrotron X-ray scattering experiments were performed at Beamline 7.3.3 of the Advanced Light Source, a U.S. DOE Office of Science User Facility under Contract No. DE-AC02-05CH11231.

Conflict of Interest

The authors declare no conflict of interest.

Data Availability Statement

The data that support the findings of this study are available from the corresponding author upon reasonable request.

Keywords

conducting polymers, deformation mechanism, mechanical properties, multiscale, viscoelasticity

Received: February 6, 2023

Revised: February 25, 2023

Published online:

- [1] K. Sim, Z. Rao, F. Ershad, C. Yu, *Adv. Mater.* **2020**, *32*, 1902417.
- [2] H. Liu, H. Zhang, W. Han, H. Lin, R. Li, J. Zhu, W. Huang, *Adv. Mater.* **2021**, *33*, 2004782.
- [3] T. J. Wallin, J. Pikul, R. F. Shepherd, *Nat. Rev. Mater.* **2018**, *3*, 84.
- [4] Q. Wang, X. Pan, C. Lin, D. Lin, Y. Ni, L. Chen, L. Huang, S. Cao, X. Ma, *Chem. Eng. J.* **2019**, *370*, 1039.
- [5] B. C. K. Tee, J. Ouyang, *Adv. Mater.* **2018**, *30*, 1802560.
- [6] S. Gao, X. Zhao, Q. Fu, T. Zhang, J. Zhu, F. Hou, J. Ni, C. Zhu, T. Li, Y. Wang, V. Murugadoss, G. A. M. Mersal, M. M. Ibrahim, Z. M. El-Bahy, M. Huang, Z. Guo, *J. Mater. Sci. Technol.* **2022**, *126*, 152.
- [7] Y. Wang, D. Yang, M. M. Hessien, K. Du, M. M. Ibrahim, Y. Su, G. A. M. Mersal, R. Ma, S. M. El-Bahy, M. Huang, Q. Yuan, B. Cui, D. Hu, *Adv. Compos. Hybrid Mater.* **2022**, *5*, 2106.
- [8] C. Lai, Y. Wang, L. Fu, H. Song, B. Liu, D. Pan, Z. Guo, I. Seok, K. Li, H. Zhang, M. Dong, *Adv. Compos. Hybrid Mater.* **2022**, *5*, 536.
- [9] H. Cheng, Y. Pan, Q. Chen, R. Che, G. Zheng, C. Liu, C. Shen, X. Liu, *Adv. Compos. Hybrid Mater.* **2021**, *4*, 505.
- [10] H. Yan, X. Dai, K. Ruan, S. Zhang, X. Shi, Y. Guo, H. Cai, J. Gu, *Adv. Compos. Hybrid Mater.* **2021**, *4*, 36.
- [11] A. Afif, S. M. H. Rahman, A. Tasfiah Azad, J. Zaini, M. A. Islan, A. K. Azad, *J. Energy Storage* **2019**, *25*, 100852.
- [12] L. Li, Y. Zhang, H. Lu, Y. Wang, J. Xu, J. Zhu, C. Zhang, T. Liu, *Nat. Commun.* **2020**, *11*, 62.
- [13] G. Li, L. Wang, X. Lei, Z. Peng, T. Wan, S. Maganti, M. Huang, V. Murugadoss, I. Seok, Q. Jiang, D. Cui, A. Alhadhrami, M. M. Ibrahim, H. Wei, *Adv. Compos. Hybrid Mater.* **2022**, *5*, 853.
- [14] S. u. Rehman, R. Ahmed, K. Ma, S. Xu, T. Tao, M. A. Aslam, M. Amir, J. Wang, *Eng. Sci.* **2021**, *13*, 71.
- [15] J. Chen, Q. Peng, T. Thundat, H. Zeng, *Chem. Mater.* **2019**, *31*, 4553.
- [16] H. He, L. Zhang, X. Guan, H. Cheng, X. Liu, S. Yu, J. Wei, J. Ouyang, *ACS Appl. Mater. Interfaces* **2019**, *11*, 26185.

- [17] W. Xie, F. Yao, H. Gu, A. Du, Q. Lei, N. Naik, Z. Guo, *Adv. Compos. Hybrid Mater.* **2022**, *5*, 1003.
- [18] J. Guo, Z. Chen, Z. M. El-Bahy, H. Liu, H. M. Abo-Dief, W. Abdul, K. M. Abualnaja, A. K. Alanazi, P. Zhang, M. Huang, G. Hu, J. Zhu, *Adv. Compos. Hybrid Mater.* **2022**, *5*, 899.
- [19] X. Xu, F. Yao, O. A. A. Ali, W. Xie, S. F. Mahmoud, P. Xie, S. M. El-Bahy, M. Huang, C. Liu, R. Fan, Z. Guo, A. Du, D. Estevez, F. Qin, H. Peng, D. P. Young, H. Gu, *Adv. Compos. Hybrid Mater.* **2022**, *5*, 2002.
- [20] J. Stejskal, *Chem. Pap.* **2020**, *74*, 1.
- [21] Y. Xu, Y. Ma, X. Ji, S. Huang, J. Xia, M. Xie, J. Yan, H. Xu, H. Li, *Appl. Surf. Sci.* **2019**, *464*, 552.
- [22] Q. Zhu, Y. Zhao, B. Miao, H. M. Abo-Dief, M. Qu, R. A. Pashameah, B. B. Xu, M. Huang, H. Algadi, X. Liu, Z. Guo, *Prog. Org. Coat.* **2022**, *172*, 107153.
- [23] K. Namsheer, C. S. Rout, *RSC Adv.* **2021**, *11*, 5659.
- [24] L. Ouyang, W. Huang, M. Huang, B. Qiu, *Adv. Compos. Hybrid Mater.* **2022**, *5*, 1126.
- [25] H. Li, W. Huang, B. Qiu, H. K. Thabet, D. Alhashmialameer, M. Huang, Z. Guo, *Adv. Compos. Hybrid Mater.* **2022**, *5*, 1888.
- [26] J. R. Reynolds, B. C. Thompson, T. A. Skotheim, *Conjugated Polymers: Properties, Processing, and Applications*, 4th ed., CRC Press, Boca Raton, FL **2019**.
- [27] D. Rodriguez, J.-H. Kim, S. E. Root, Z. Fei, P. Boufflet, M. Heeney, T.-S. Kim, D. J. Lipomi, *ACS Appl. Mater. Interfaces* **2017**, *9*, 8855.
- [28] R. F. Landel, L. E. Nielsen, *Mechanical Properties of Polymers and Composites*, 2nd ed., CRC Press, Boca Raton, FL **1993**.
- [29] L. H. Sperling, *Introduction to Physical Polymer Science*, John Wiley & Sons, Inc., Hoboken, NJ **2005**, pp. 507–556.
- [30] J.-Y. Sun, X. Zhao, W. R. K. Illeperuma, O. Chaudhuri, K. H. Oh, D. J. Mooney, J. J. Vlassak, Z. Suo, *Nature* **2012**, *489*, 133.
- [31] T. L. Sun, T. Kurokawa, S. Kuroda, A. B. Ihsan, T. Akasaki, K. Sato, M. A. Haque, T. Nakajima, J. P. Gong, *Nat. Mater.* **2013**, *12*, 932.
- [32] E. Filippidi, T. R. Cristiani, C. D. Eisenbach, J. H. Waite, J. N. Israelachvili, B. K. Ahn, M. T. Valentine, *Science* **2017**, *358*, 502.
- [33] J. Wu, L.-H. Cai, D. A. Weitz, *Adv. Mater.* **2017**, *29*, 1702616.
- [34] Q. Zhang, C.-Y. Shi, D.-H. Qu, Y.-T. Long, B. L. Feringa, H. Tian, *Sci. Adv.* **2018**, *4*, eaat8192.
- [35] T. Matsuda, R. Kawakami, R. Namba, T. Nakajima, J. P. Gong, *Science* **2019**, *363*, 504.
- [36] W. Wang, X. Zhang, N. Chou, Z. Li, Y. Shi, *Compos. Struct.* **2018**, *200*, 135.
- [37] J. Tsai, C. T. Sun, *Compos. Sci. Technol.* **2002**, *62*, 1289.
- [38] Y. Wang, S. Wang, C. Xu, S. Xuan, W. Jiang, X. Gong, *Compos. Sci. Technol.* **2016**, *127*, 169.
- [39] Y. Qiu, L. Wu, S. Liu, W. Yu, *ACS Appl. Mater. Interfaces* **2023**, *15*, 10053.
- [40] J. T. Fan, J. Weerheijm, L. J. Sluys, *Polymer* **2015**, *65*, 72.
- [41] N. Y. C. Lin, C. Ness, M. E. Cates, J. Sun, I. Cohen, *Proc. Natl. Acad. Sci. USA* **2016**, *113*, 10774.
- [42] S. Gürgeç, M. C. Kuşhan, W. Li, *Prog. Polym. Sci.* **2017**, *75*, 48.
- [43] K. Song, W. Huang, H. Wan, H. Huang, *IOP Conf. Ser.: Mater. Sci. Eng.* **2017**, *207*, 012024.
- [44] J. W. van Egmond, *Curr. Opin. Colloid Interface Sci.* **1998**, *3*, 385.
- [45] R. C. W. Liu, Y. Morishima, F. M. Winnik, *Macromolecules* **2001**, *34*, 9117.
- [46] R. C. W. Liu, Y. Morishima, F. M. Winnik, *Macromolecules* **2003**, *36*, 4967.
- [47] C. Chassenieux, T. Nicolai, L. Benyahia, *Curr. Opin. Colloid Interface Sci.* **2011**, *16*, 18.
- [48] J. Wang, L. Benyahia, C. Chassenieux, J.-F. Tassin, T. Nicolai, *Polymer* **2010**, *51*, 1964.
- [49] A. G. MacDiarmid, A. J. Epstein, *Synth. Met.* **1995**, *69*, 85.
- [50] H. D. Tran, J. M. D'Arcy, Y. Wang, P. J. Beltramo, V. A. Strong, R. B. Kaner, *J. Mater. Chem.* **2011**, *21*, 3534.
- [51] H. S. Kolla, S. P. Surwade, X. Zhang, A. G. MacDiarmid, S. K. Manohar, *J. Am. Chem. Soc.* **2005**, *127*, 16770.
- [52] M. Sezen-Edmonds, Y.-L. Loo, *J. Phys. Chem. Lett.* **2017**, *8*, 4530.
- [53] R. J. Murphy, K. M. Weigandt, D. Uhrig, A. Alsayed, C. Badre, L. Hough, M. Muthukumar, *Macromolecules* **2015**, *48*, 8989.
- [54] T. Takano, H. Masunaga, A. Fujiwara, H. Okuzaki, T. Sasaki, *Macromolecules* **2012**, *45*, 3859.
- [55] J. Ouyang, *Displays* **2013**, *34*, 423.
- [56] L. V. Kayser, D. J. Lipomi, *Adv. Mater.* **2019**, *31*, 1806133.
- [57] P. Ge, Q. Cai, H. Zhang, X. Yao, W. Zhu, *ACS Appl. Mater. Interfaces* **2020**, *12*, 37549.
- [58] G. Lalevé, L. David, A. Montembault, K. Blanchard, J. Meadows, S. Malaise, A. Crépet, I. Grillo, I. Morfin, T. Delair, G. Sudre, *Soft Matter* **2017**, *13*, 6594.
- [59] W. E. Dondero, R. E. Gorga, *J. Polym. Sci., Part B: Polym. Phys.* **2006**, *44*, 864.
- [60] M. Gu, W.-J. Song, J. Hong, S. Y. Kim, T. J. Shin, N. A. Kotov, S. Park, B.-S. Kim, *Sci. Adv.* **2019**, *5*, eaaw1879.
- [61] A. A. Krauskopf, A. M. Jimenez, E. A. Lewis, B. D. Vogt, A. J. Müller, S. K. Kumar, *ACS Macro Lett.* **2020**, *9*, 1007.
- [62] N. Kim, S. Kee, S. H. Lee, B. H. Lee, Y. H. Kahng, Y.-R. Jo, B.-J. Kim, K. Lee, *Adv. Mater.* **2014**, *26*, 2268.
- [63] K. E. Aasmundtveit, E. J. Samuelsen, L. A. A. Pettersson, O. Inganäs, T. Johansson, R. Feidenhans'l, *Synth. Met.* **1999**, *101*, 561.
- [64] J. P. Gong, *Soft Matter* **2010**, *6*, 2583.
- [65] G. E. Fantner, T. Hassenkam, J. H. Kindt, J. C. Weaver, H. Birkedal, L. Pechenik, J. A. Cutroni, G. A. G. Cidade, G. D. Stucky, D. E. Morse, P. K. Hansma, *Nat. Mater.* **2005**, *4*, 612.
- [66] M. Hua, S. Wu, Y. Ma, Y. Zhao, Z. Chen, I. Frenkel, J. Strzalka, H. Zhou, X. Zhu, X. He, *Nature* **2021**, *590*, 594.
- [67] Y. Huang, D. R. King, T. L. Sun, T. Nonoyama, T. Kurokawa, T. Nakajima, J. P. Gong, *Adv. Funct. Mater.* **2017**, *27*, 1605350.
- [68] S. Lin, C. Cao, Q. Wang, M. Gonzalez, J. E. Dolbow, X. Zhao, *Soft Matter* **2014**, *10*, 7519.
- [69] D. R. King, T. Okumura, R. Takahashi, T. Kurokawa, J. P. Gong, *ACS Appl. Mater. Interfaces* **2019**, *11*, 35343.
- [70] J. Cui, S. Wang, S. Wang, G. Li, P. Wang, C. Liang, *Polymers* **2019**, *11*.
- [71] G. Zhang, Q. Zhao, W. Zou, Y. Luo, T. Xie, *Adv. Funct. Mater.* **2016**, *26*, 931.
- [72] J. Wu, Y. Wang, J. Zhang, C. Zhao, Z. Fan, Q. Shu, X. He, S. Xuan, X. Gong, *Matter* **2022**, *5*, 2265.
- [73] B. Yan, J. Huang, L. Han, L. Gong, L. Li, J. N. Israelachvili, H. Zeng, *ACS Nano* **2017**, *11*, 11074.
- [74] J.-F. Yin, H. Xiao, P. Xu, J. Yang, Z. Fan, Y. Ke, X. Ouyang, G. X. Liu, T. L. Sun, L. Tang, S. Z. D. Cheng, P. Yin, *Angew. Chem., Int. Ed.* **2021**, *60*, 22212.
- [75] C. S. Boland, U. Khan, G. Ryan, S. Barwich, R. Charifou, A. Harvey, C. Backes, Z. Li, M. S. Ferreira, M. E. Möbius, R. J. Young, J. N. Coleman, *Science* **2016**, *354*, 1257.
- [76] N. Iqbal, M. Tripathi, S. Parthasarathy, D. Kumar, P. K. Roy, *RSC Adv.* **2016**, *6*, 109706.
- [77] S. Yao, Y. Zhu, *Adv. Mater.* **2015**, *27*, 1480.
- [78] N. Matsuhisa, D. Inoue, P. Zalar, H. Jin, Y. Matsuba, A. Itoh, T. Yokota, D. Hashizume, T. Someya, *Nat. Mater.* **2017**, *16*, 834.
- [79] L. Li, Q. Lin, M. Tang, A. J. E. Duncan, C. Ke, *Chemistry* **2019**, *25*, 10768.